SUBCONTRACT TITLE**:** **Fabrication and Physics of CdTe Devices by Sputtering**

SUBCONTRACT TITLE**:** **RXL-5-44205-01**

QUARTERLY TECHNICAL STATUS REPORT FOR**:**

Phase 2/Quarter 3

SUBMITTED TO**:** **Bolko von Roedern**
National Renewable Energy Laboratory

PRINCIPAL INVESTIGATORS:

A.D. Compaan (P.I.),
R.W. Collins (co-P.I.), V.G. Karpov (co-P.I.)
Department of Physics and Astronomy,
2801 W Bancroft,
Toledo, OH 43606

This progress report covers the Third Quarter of Phase 2 for the period from

December 1, 2006 through February 28, 2007,

of the above Thin Film Photovoltaic Partnership Program subcontract.
The focus of research during this quarter was on back contact development and on the advanced analysis of CdS using real time spectroscopic ellipsometry and its potential applications for monitoring of production lines for CdTe solar cell fabrication.

Contents

1. Transparent Back Contacts, and the Effect of ITO Conductivity

Task 2.1.1 Buffer and Interface Layers

HRT's first applied in Task 1.1.2 will be further developed in conjunction with Cu and Cu-free back contact.

Transparent back contacts are useful for at least two reasons. First, if the transparent back contact is a p+/n+ structure, then it would be identical to a recombination junction in a monolithically integrated double junction tandem cell. It is possible to make a single junction cell that is only the top half of such a cell, and optimize this top half separately. Secondly, not only do transparent back contacts allow characterization from the "sunny" (also called front) side, as usual in solar cells, but they also allow characterization from the contact (back) side to further illuminate the internal physics of the device.

During this quarter, we studied CdS/CdTe solar cells with 2.3μm CdTe (our standard laboratory thickness) prepared with four different types of p+/n+ transparent back contacts (TBCs). We have used ZnTe:Cu and ZnTe:N as the p-type materials, and ZnO:Al and Indium Tin Oxide (ITO) as the n-type materials. This gives rise to four possible combinations: ZnTe:Cu/ZnO:Al, ZnTe:N/ZnO:Al, ZnTe:Cu/ITO, and ZnTe:N/ITO. ZnTe:N/ITO was found to give the best results. Figure 1 shows the cell structure.

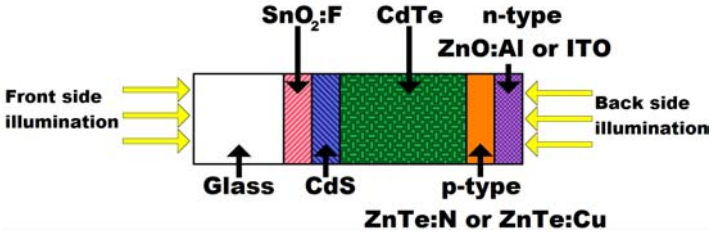

Figure 1. Cell structure and meaning of front and back side illumination

All cells were prepared on commercially available Pilkington TEC 7 fluorine-doped tin-oxide-coated soda-lime glass. All subsequent layers were deposited with RF sputtering and, excepting the reactively sputtered ZnTe:N, in pure argon atmospheres. CdS and CdTe were deposited at 250°C and 18 mTorr argon pressure. CdS and CdTe were deposited with 35 and 20 watts rf power, respectively. All samples used nominally the same 0.13 μm thickness of CdS. After CdS/CdTe deposition, 2.3μm samples were $CdCl_2$ treated at 387°C for 30 minutes. After $CdCl_2$ treatment, either ZnTe:N was deposited by using an undoped ZnTe target and reactively sputtering in a 5% nitrogen-95% argon environment, or ZnTe:Cu was deposited by using a target doped with 2% copper by weight. In both cases, the layer was deposited with a substrate temperature of 325°C. We finally deposited an n-type transparent conductive oxide, ITO or ZnO:Al. The ITO target was 90% In_2O_3 and 10% SnO_2 by weight. For the ZnTe:Cu/ITO contact, ITO was deposited at 150°C. For the ZnTe:N/ITO contact, ITO was deposited at various temperatures. (See below.) The ZnO:Al target was doped with 2% Al_2O_3 by weight. ZnO:Al was deposited at 200°C.

Figure 2a shows the J-V curves (with standard front illumination) for cells with ZnO:Al as the n-type contact. Of the contacts used in our study, ZnTe:N/ZnO:Al gives the poorest performance, with open-circuit voltage being particularly low. While the ZnTe:Cu/ZnO:Al contact has a reasonable open-circuit voltage, close to that of CdTe cells containing copper, the large series resistance (23 ohm-cm^2) decreases the fill factor, which is the greatest limitation to its the efficiency as compared to ZnTe:N/ITO cells. (See below.)

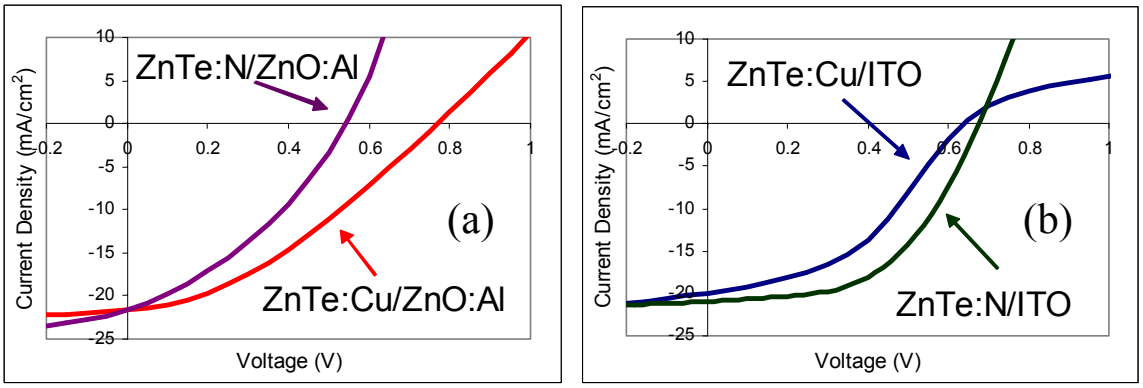

Figure 2. J-V data for cells with 2.3 μm CdTe, illuminated from the front side with n-type contact of: (a) ZnO:Al and (b) ITO.

Figure 2b shows the J-V curves for cells with ITO as the n-type contact. For cells with ZnTe:Cu as the p-type layer, the most dramatic difference here from the cells with ZnO:Al is the rollover in the first quadrant in the ITO case. This is typical of a back contact barrier that can result from poor valence band alignment at the back contact. ZnTe:N/ITO gives the best overall results.

The second level metrics of the best cells with each back contact are summarized in Table *1*.

Table 1. Efficiency and second-level metrics for CdTe cells with transparent contacts.

Back Contact	**Voc (mV)**	**Jsc (mA/cm^2)**	**Fill Factor (%)**	**Efficiency (%)**
ZnTe:Cu/ZnO:Al	762	20.8	38	6.1
ZnTe:Cu/ITO	640	17.7	43	4.9
ZnTe:N/ZnO:Al	543	21.6	35	4.1
ZnTe:N/ITO	676	21	53	7.5

Optimizing ITO conductivity for back contacts—The results shown in Table 1 and Figure 2 were obtained after some optimization of the ITO conductivity. We used substrate temperature to control the conductivity of the ITO. Figure 3 shows the increase in conductivity, over three orders of magnitude, of ITO films deposited on glass as the substrate temperature is increased from 25 °C to 300 °C.

Although intuitively one might expect the best solar cells to use transparent back contacts with the greatest conductivity, we have observed that this is not the case. Fig. 4 shows J-V curves (using front illumination) of 2.3 μm CdTe and a ZnTe:N/ITO back contact for ITO deposition temperatures of 50 ^{o}C, 170 ^{o}C and 300 ^{o}C. a) For low

deposition temperature (50°C) ITO, the open-circuit voltage is similar to the intermediate and high temperature cases, but the efficiency is limited by the large series resistance, lowering the short-circuit current and reducing the fill factor essentially to 25%. b) In the case of intermediate temperature deposition (170°C), good overall parameters are

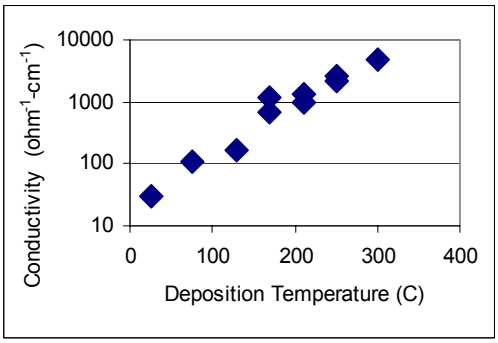

Figure 3. Variation of ITO conductivity with deposition temperature.

obtained. c) When the temperature is increased to the highest temperature we studied (300°C), the performance does not continue to increase. "Roll-under" appears in the fourth quadrant that reduces the fill factor to less than 25%. We found that such cells also usually have higher efficiency when illuminated from the back side than from the front. We believe these problems are not due to subjecting the entire cell to high temperature in the final stage of the deposition, for the following reasons: 1) The deposition of ZnTe:N just prior to ITO is done at even higher temperature (325°C). 2) It is possible to measure J-V curves through the ZnTe:N, off the ITO contacts, and while current collection is very poor, no rollunder or rollover is observed. 3) Finally, it is possible, on a given plate, first to deposit contacts under the high temperature condition and then perform a second deposition of contacts at the intermediate temperature condition between the previously existing (high temperature) ITO contacts, and the behavior of the different series of cells is what would be obtained with a single deposition. We speculate that the development of roll under is caused by poor band alignment between the ZnTe:N and the higher temperature deposited ITO, as the electron affinity of ITO may change with preparation conditions.

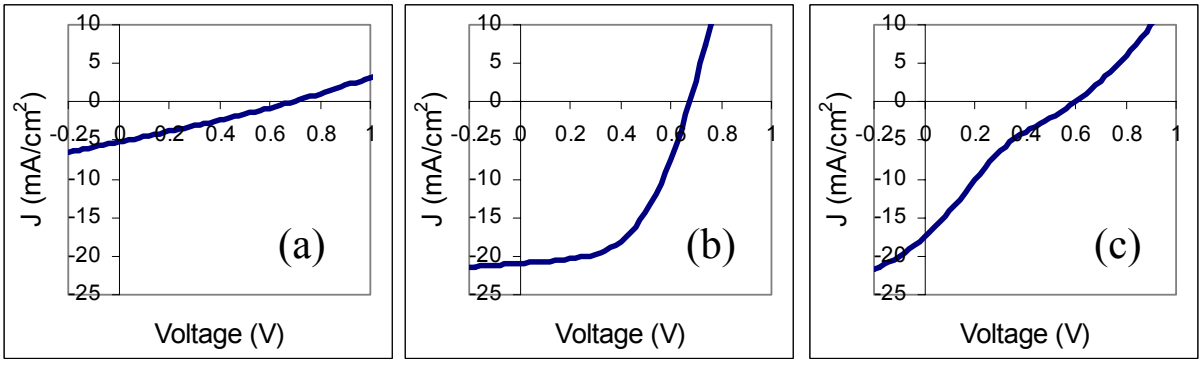

Figure 4. J-V curves of CdTe/ZnTe:N/ITO cells using (a) 50 °C ITO, (b) 170 °C ITO, and (c) 300 °C ITO.

2. Real Time Spectroscopic Ellipsometry

Task 3.1.3
Effects of Morphology and Grain Boundaries

Real time SE will be applied to study the morphology of CdS growth.

The real time spectroscopic ellipsometry (SE) studies of the growth and grain structure of CdS will be reported under Task 3.3.2.

Task 3.3.2
Real Time Spectroscopic Ellipsometry

Real time SE will be applied in a number of materials fabrication tasks, with the emphases on characterizing the $CdCl_2$ treatment and analysis of the morphological evolution of CdS and its interaction with various substrate materials.

2.1 Motivation

There are two goals of real time SE studies of CdS morphological development. The first goal is to achieve a better understanding of the processing-property relationships in CdTe solar cells so that they can be designed rationally for higher efficiency. The second goal is to establish the methodology required to extract the maximum possible information when SE is applied as a spatially resolved mapping tool on the CdTe solar cell production line. Figure 5 shows the optical geometry that is anticipated for such a mapping instrument. Focusing optics are needed in order to avoid collecting the top surface reflection from the glass substrate which is not of interest. In addition, this beam is incoherent relative to the light beam of interest which is reflected at the interface between the coated glass and the solar cell.

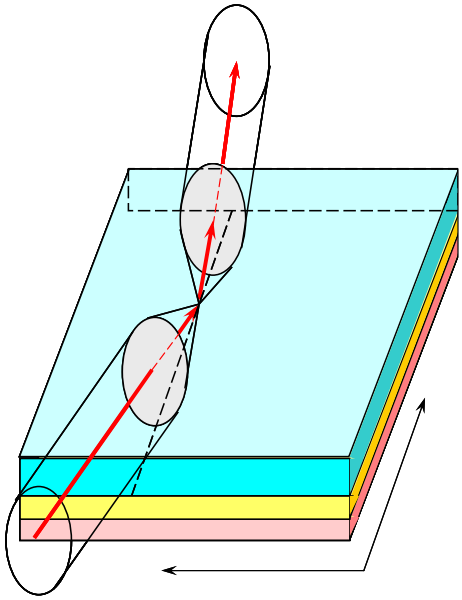

Figure 5. Mapping SE configuration with focusing optics to collect reflection from the (TEC glass)/(solar cell) interface.

2.2 Progress in the Development of On-Line Monitoring

Research to assess the capability of SE for on-line monitoring has begun. In this effort, the top surface reflection has been eliminated by optically contacting a 60° prism to the glass surface. Although this approach cannot be applied in on-line applications, it is suitable for assessing the information content that can be extracted upon development

of the focusing approach of Figure 5. In order to provide a second check on this information, SE has also been performed from the back (CdTe) side of the same solar cell. The geometries of the glass side and CdTe side measurements are shown in Figure 6. In

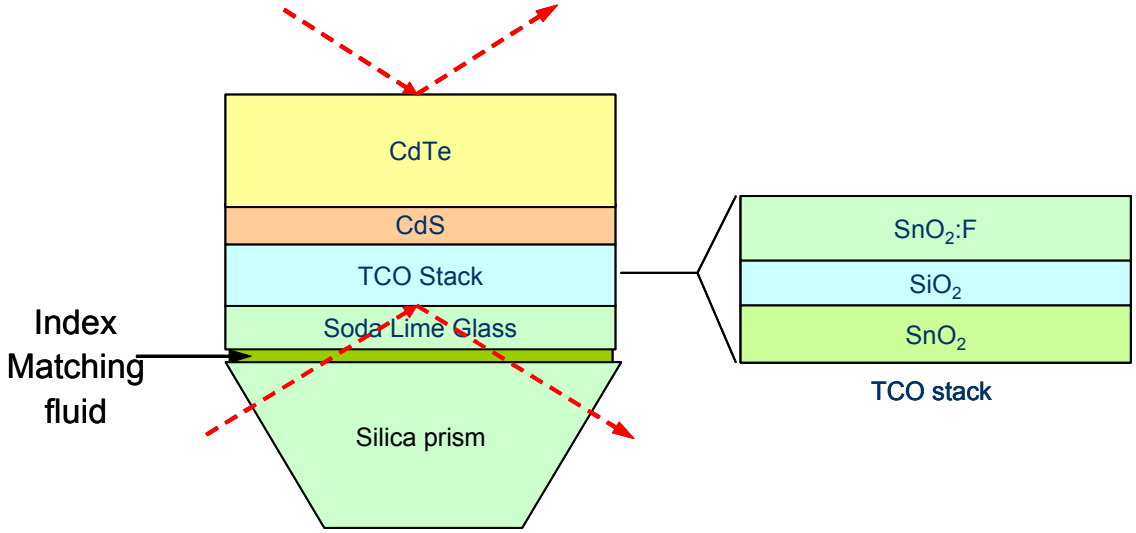

Figure 6. Optical configuration for ex situ SE data acquisition from the CdTe free surface after etching steps and from the prism/glass substrate side without CdTe etching.

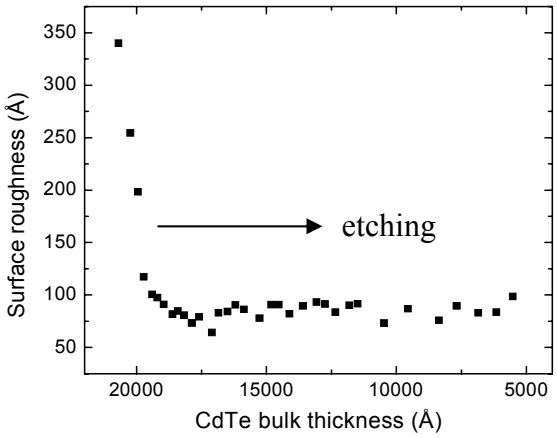

Figure 7. The smoothening effect of Br_2+methanol etching of CdTe.

order to measure from the CdTe side, the CdTe surface is exposed to a Br_2 etch (0.05 vol.% Br_2 in methanol), which is performed after the $CdCl_2$ treatment, but before back contact formation. The role of this etch is to remove the surface oxide layer, reduce the roughness, and provide a means for depth profiling through the bulk CdTe thickness. The bulk CdTe thickness removed per etching step can be controlled by the Br_2 concentration and etching time. After each etching step, the sample was rinsed with methanol, and then continuously blown with Ar gas during measurement to minimize reoxidation. The smoothening effect of the Br_2+methanol etch is evident in Figure 7. Roughness layer thicknesses after etching as small as ~20 Å are possible by optimizing this method.

A dielectric function library, deduced as described in previous reports, was used in the analysis of the ex situ SE data acquired after $CdCl_2$ treatment, but before back contact formation for a CdTe solar cell prepared by sputtering on TEC-15 glass. Measurements of the same sample have been performed on the prism/glass substrate side (see Figure 8)

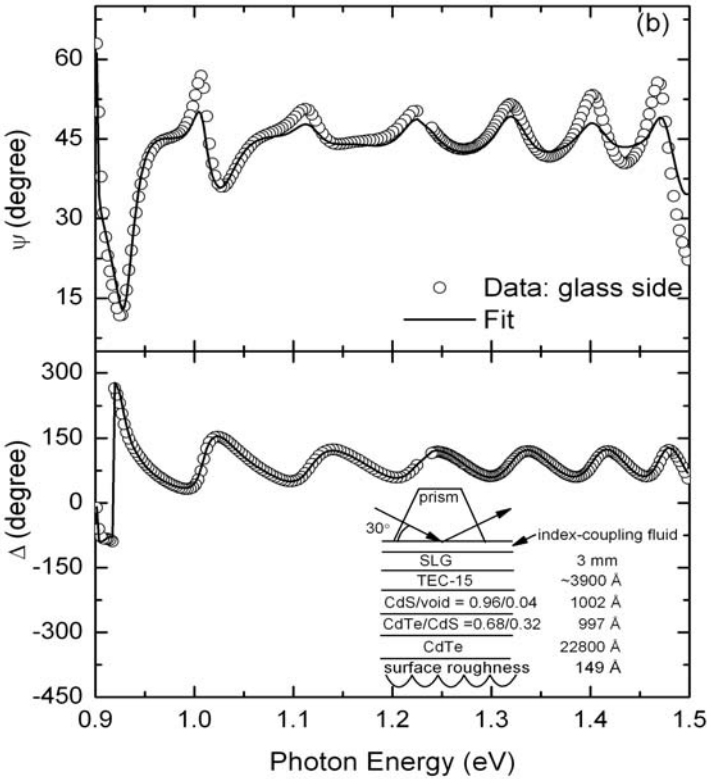

Figure 8. Ex situ SE spectra in (ψ, Δ) (symbols) for a CdTe solar cell after $CdCl_2$ treatment, but before back contact formation, as measured from the prism/glass side. The best fit results (solid lines) yield the structural parameters in the inset.

and on the CdTe free surface, the latter after 8 etching steps (see Figure 9). The dielectric function library is continuously being refined for improved fitting of such ex situ SE data on the nearly complete devices. The results of the fits (solid lines) to the (ψ, Δ) spectra (symbols) obtained with the current library are shown in Figures 8 and 9. The structural model used in the analysis of both data sets is the same and includes (from film to substrate side): (i) a CdTe surface roughness layer; (ii) a CdTe bulk layer; (iii) an (interface-roughness + interdiffusion) region between the CdTe and CdS, modeled for simplicity as a physical mixture to simulate an assumed dominant interface roughness effect; (iv) CdS with a variable void volume fraction; (v) an interface roughness layer between CdS and the SnO_2:F of TEC-15; and (vi) the TEC-15 structure.

The insets of Figures 8 and 9 show the multilayer models of the structure, the former depicting the placement of a 60° fused silica prism on top of the superstrate. In this configuration, an index-matching fluid proves vital in eliminating unwanted incoherent reflections and making good fits possible. Considering the assumptions and simplifications of the model, the agreement in the structural parameters listed in the two insets is significant. (Note that agreement in the CdTe bulk and roughness thicknesses is

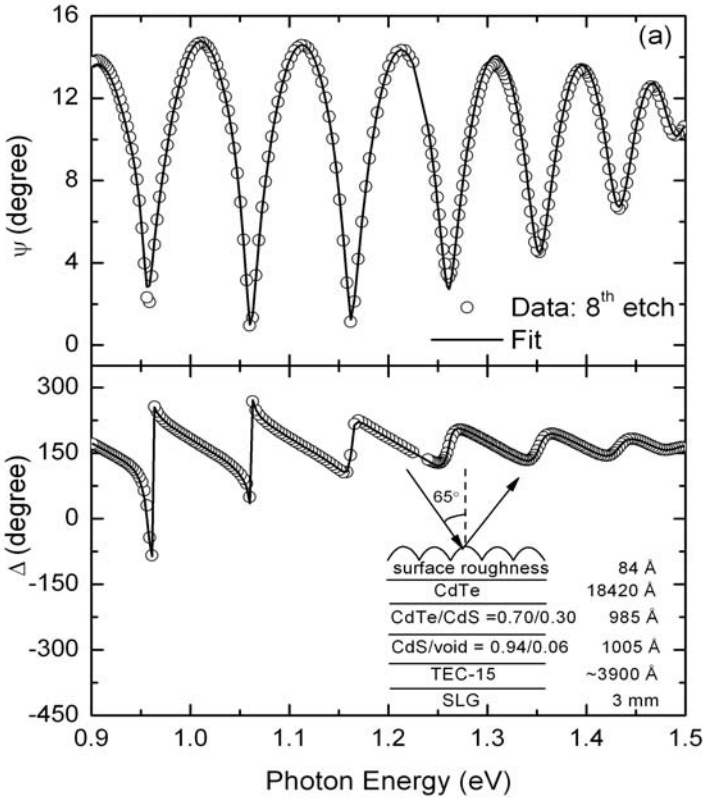

Figure 9. Ex situ SE spectra in (ψ, Δ) (symbols) from the free CdTe surface after 8 Br_2+methanol etching steps. The best fit results (solid lines) yield the structural parameters in the insets.

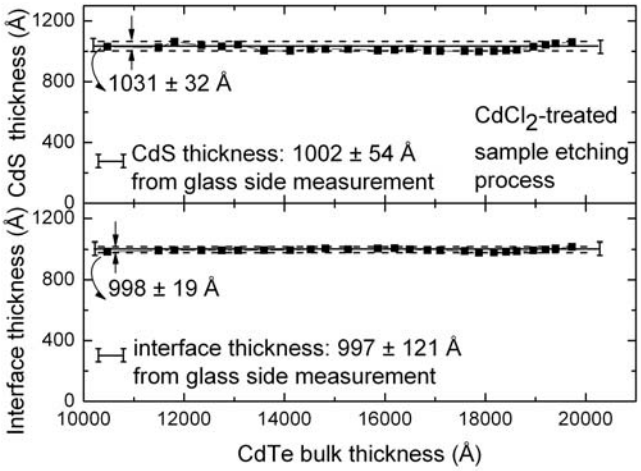

Figure 10. CdS and CdTe/CdS interface layer thicknesses deduced from spectra collected through the prism/glass (solid line) and from spectra collected from the CdTe surface in successive etches (points, dotted line extrema).

not expected since the CdTe film has been etched for the back side measurements.) Good agreement is obtained in the CdTe/CdS composition even though this layer requires a more complex modeling approach that includes inter-diffusion [1]. As final supporting results for the overall approach, the CdS layer and CdTe/CdS interface thicknesses deduced from spectra collected at the CdTe free surface in 24 successive etches shown in Figure 10 exhibit ~ ±1-1.5% deviations and the average values lie within the confidence limits of the analyses performed on spectra collected through the prism/glass.

2.3 CdS Morphology and Optical Properties

One of the primary weaknesses of the fitting procedure, described in conjunction with Figures 8-10, is the variability in the CdS dielectric function due to changes in the substrate nature and detailed deposition and post-process conditions. Although voids are being used currently to account for sample-to-sample variations in CdS structure, it has been recognized that a more sophisticated approach is required. This approach can be developed starting from a study of CdS films sputter deposited at different temperatures.

The series of CdS thin films studied here was deposited on c-Si wafers at substrate temperatures T over the range from 145°C to 320°C. All other parameters were fixed (rf power = 50 W, Ar pressure = 10 mTorr, Ar flow = 23 sccm). Further details on the experimental real time SE setup can be found in the Phase 2 Quarter 1 Report. Previously we suggested that the grain size of as-deposited CdS shows a strong dependence on deposition temperature, as seen from the widths of the critical points (CP's) in the optical properties of the hexagonal CdS (see Figure 11 below). In this work we have quantified this dependence, and from the observed consistent variations in width for the different CP's, important information could be deduced, including (i) the average grain size of the

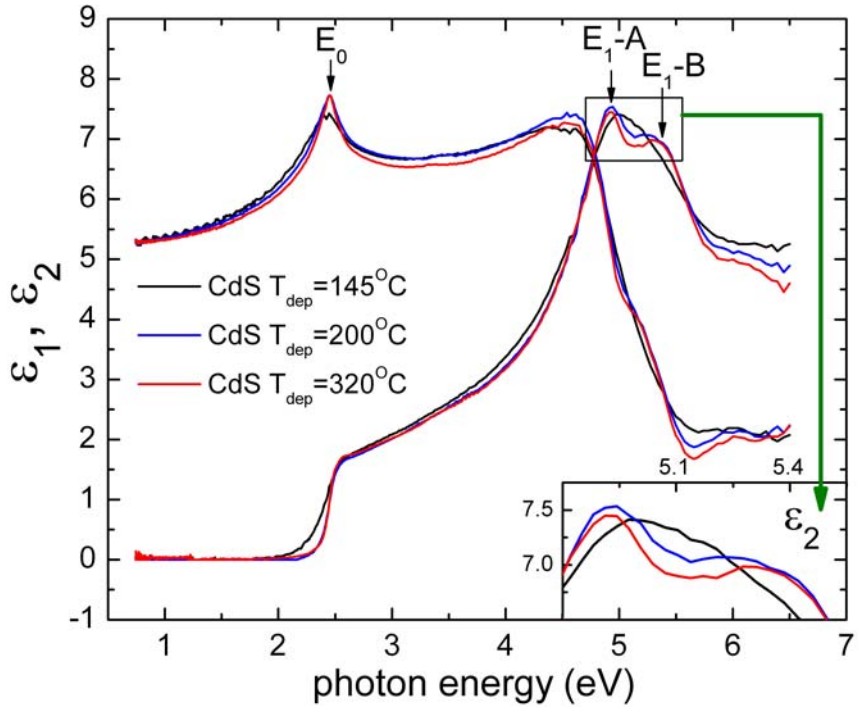

Figure 11. Dielectric functions measured at ~15°C for CdS films magnetron sputter-deposited at three different temperatures.

film (obtained in this case as a function of substrate temperature) and (ii) the group speeds of the electronic excitations in CdS. Once the group speeds are obtained, the optical properties for any hexagonal CdS film can be interpreted to deduce the grain size.

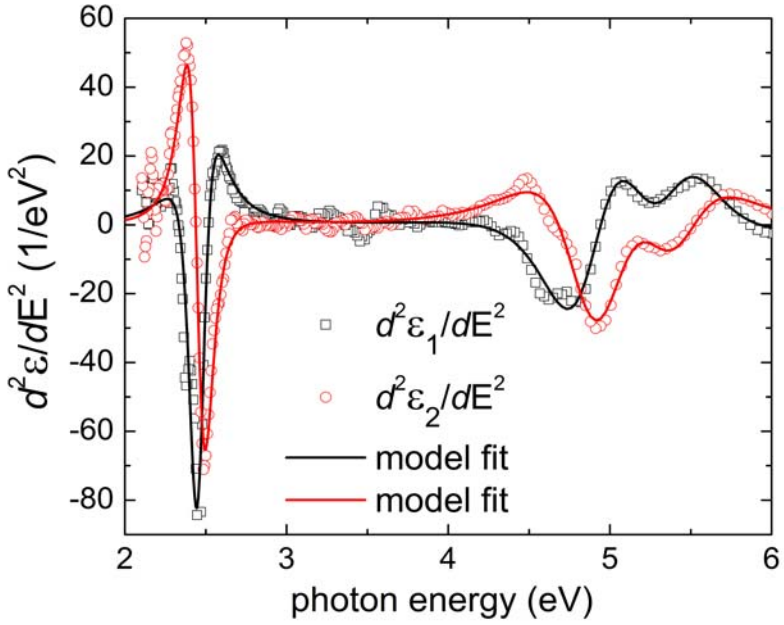

Figure 12. Second derivative spectra (open squares and circles) in ε for CdS deposited at T=160°C and measured at T~15°C. The fit (solid lines) is based on Equation (1).

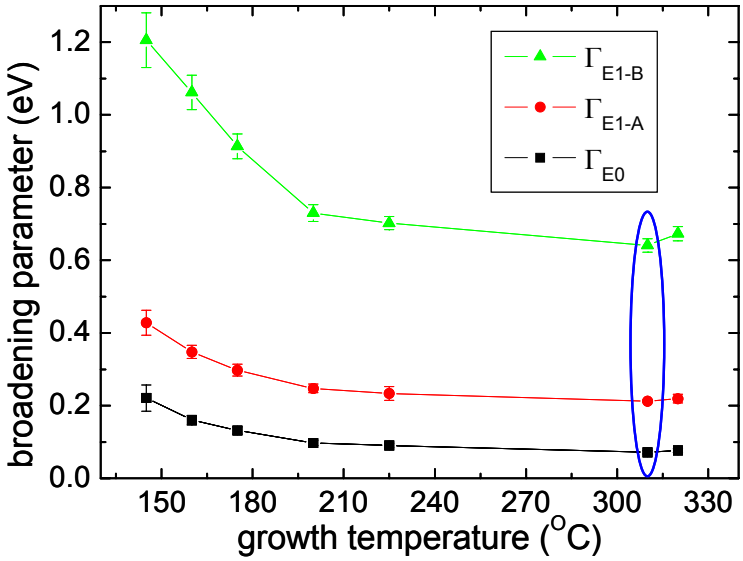

Figure 13. Broadening parameters measured at ~15°C for CdS films deposited at different T; the lowest broadening parameter values are circled.

As shown in Figures 11 and 12, the E_0 (fundamental gap), E_1-A, and E_1-B CP's are evident in the T~15°C dielectric functions ε of the CdS samples [2]. To quantify the CP's, the second derivative spectra in ε were fit assuming the parabolic band approximation to the critical points (CP-PB):

$$\varepsilon = \sum_n A_n (E - E_n - i\Gamma_n)^{\mu_n} \exp(i\varphi_n) \qquad (1)$$

where A_n, E_n, Γ_n, μ_n, and φ_n are the amplitude, band gap, broadening parameter, exponent, and phase of the n^{th} CP, respectively [3]. One such fit is shown in Figure 12.

The best fit broadening parameter Γ_n is plotted as a function of deposition temperature T in Figure 13. The variations of Γ_n with T for all CP's are quite consistent. The dielectric function for the sample deposited at 310°C with the smallest Γ_n (circled in Figure 13) has been used as a reference dielectric function in the modeling of Figures 8-10. Figure 14 shows comparisons between of the dielectric functions of the thin films and the ordinary component of the dielectric function of hexagonal single crystal CdS. The similar features of the spectra -- including the appearance of the (E_1-A, E_1-B) doublet -- suggest that the thin film measurement probes the ordinary dielectric function of hexagonal CdS. This would suggest that the film is crystallographically oriented with its c-axis normal to the surface. It can be seen in Figure 14 that the CP features of the

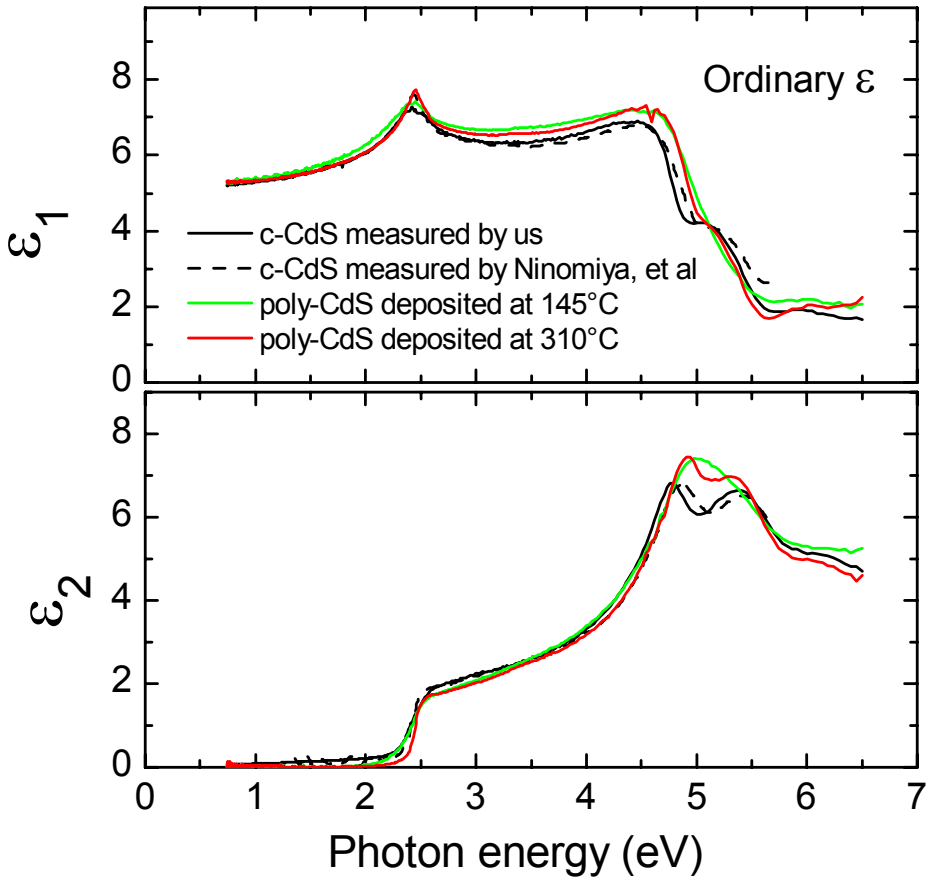

Figure 14. Comparison of the ordinary dielectric function of hexagonal single crystal CdS and two polycrystalline CdS thin films deposited in this study.

dielectric function for this sample are even sharper than those of single crystal hexagonal CdS measured in this study as well as by Ninomiya et al. [2]. The broader critical points for the single crystal are likely due to defects from polishing, e.g., dislocations, that extend well below the surface. Thus, Γ_n for the 310°C sample can be taken as intrinsic to single crystal CdS (denoted by Γ_{bn}) -- even more so than results from careful measurements on single crystal CdS itself. Thus, the E_0 transition for this sample can be related to the band structure of CdS, shown schematically in Figure 15. Here the broadening parameter associated with the fundamental gap, Γ_{b0}, indicates how far away from the Brillouin zone center an excitation can occur and still contribute significantly to the optical transitions at E_0. Assuming the parabolic band approximation for the E_0 transition with electron and hole effective masses of $m_e^* = 0.2m_e$ and $m_h^* = 0.7m_e$ [4], the group speed associated with this excitation can be estimated as $v_{g0} \sim 2.2 \times 10^5$ m/s. If the dominant broadening effect is assumed to result from the limited excitation lifetime due to grain boundary scattering, then the following relation can be applied:

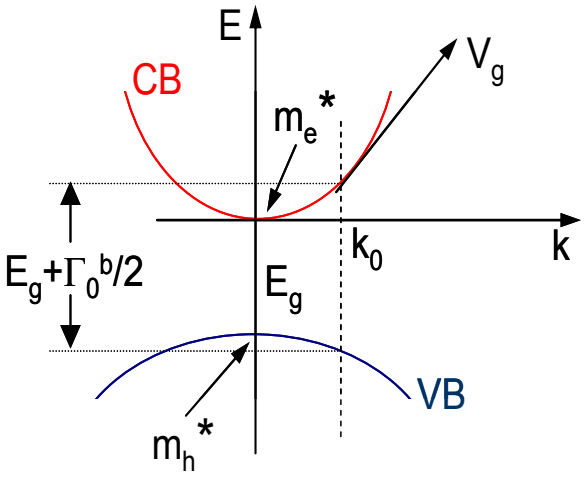

Figure 15. Schematic band diagram of a direct gap semiconductor (such as CdS) around the fundamental gap E_0.

$$\Gamma_n = \Gamma_{bn} + h v_{gn}/R \qquad (2)$$

where R is the deduced grain radius [5]. Using the values of v_{g0} and Γ_{b0} for single crystal CdS, R can be calculated as versus T as shown in Figure 16. As a check of the validity of

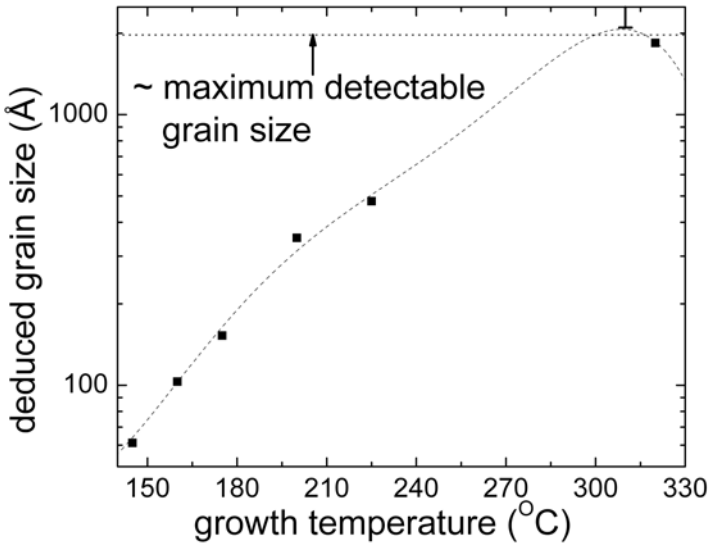

Figure 16. Grain size in CdS thin films estimated from the broadening parameter of the E_0 transition by using the inverted form of Equation (2).

the general approach, the other two critical point widths $\Gamma_{E1\text{-}A}$ and $\Gamma_{E1\text{-}B}$ are plotted versus R^{-1} in Figure 17. The linear relation predicted by Equation (2) is closely followed. From the linear fits, the group speeds for the E_1-A and E_1-B excitations are estimated to be 3.3×10^5 and 8.8×10^5 m/s respectively.

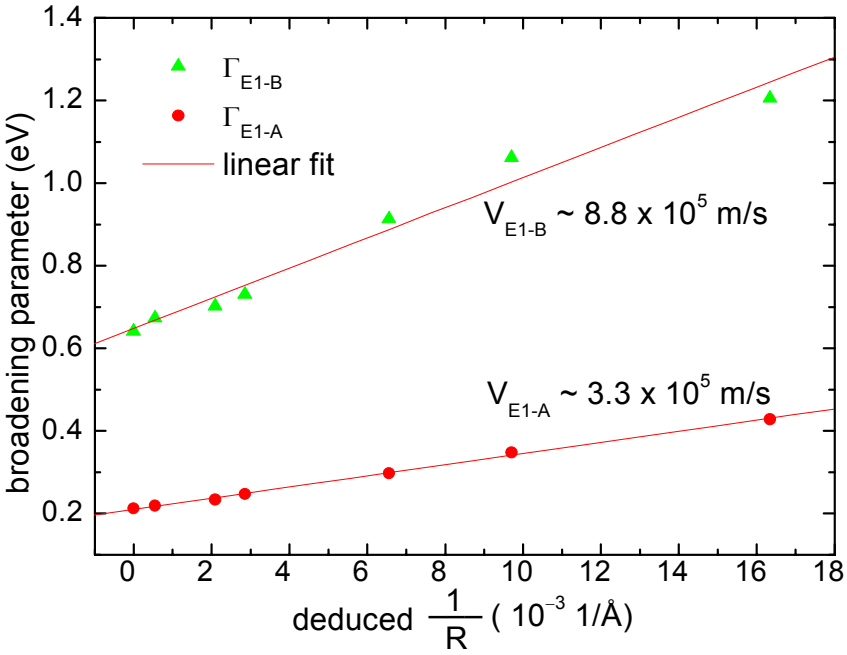

Figure 17. Broadening parameters of the E_1-A and E_1-B CPs vs. inverse grain size; group speeds calculated from the linear fits and Equation (2) are indicated.

With this information, a dielectric function parameterization is possible that uses the grain size as a controlling parameter -- similar to what is now possible with void fraction. In this parameterization the grain size is assigned, and using the known values of Γ_{bn} and v_n, then the Γ_n values can be determined according to Eq. (2). Once the Γ_n values are determined, they are substituted along with the other parameters associated with the T=310°C film into Eq. (1) to determine the dielectric function of a film with a given grain size. This is one of a few steps needed to extract physical parameters, including void fraction, grain size, and strain, from an ex situ measurement of the nearly complete solar cell with an on-line mapping capability.

References

[1] B.E. McCandless, G.M. Hanket, D.G. Jensen, and R.W. Birkmire, *J. Vac. Sci. Technol. A* **20**, 1462 (2002).
[2] S. Ninomiya and S. Adachi, *J. Appl. Phys*. **78**, 1183 (1995).
[3] R.W. Collins and A.S. Ferlauto, in *Handbook of Ellipsometry*, edited by H.G. Tompkins and E.A. Irene, (William Andrew, Norwich NY, 2005), p. 152.
[4] J.I. Pankove, *Optical Processes in Semiconductors*, (Dover, New York, 1975).
[5] G.F. Feng and R. Zallen, *Phys. Rev. B* **40**, 1064 (1989).